Numerical modeling of extreme rogue waves generated by directional energy focusing

Christophe Fochesato, Stéphan Grilli, Frédéric Dias [a,b,c]

[a] *Mathématiques Appliquées de Bordeaux, Université de Bordeaux, 351 Cours de la Libération, 33405 Talence cedex, France*

[b] *Ocean Engineering Department, University of Rhode Island, Narragansett, RI, U.S.A.*

[c] *Centre de Mathématiques et de Leurs Applications, Ecole Normale Supérieure de Cachan, 61 avenue du Président Wilson, 94235 Cachan cedex, France*

Abstract

Three-dimensional (3D) directional wave focusing is one of the mechanisms that contributes to the generation of extreme waves, also known as rogue waves, in the ocean. To simulate and analyze this phenomenon, we generate extreme waves in a 3D numerical wave tank (NWT), by specifying the motion of a snake wavemaker. The NWT solves fully nonlinear potential flow equations with a free surface, using a high-order boundary element method and a mixed Eulerian-Lagrangian time updating. Some numerical aspects of the NWT were recently improved, such as the accurate computation of higher-order derivatives on the free surface and the implementation of a fast multipole algorithm in the spatial solver. The former has allowed the accurate simulation of 3D overturning waves and the latter has led to at least a one-order of magnitude increase in the NWT computational efficiency. This made it possible to generate finely resolved 3D focused overturning waves and analyze their geometry and kinematics. In this paper, we first summarize the NWT equations and numerical methods. We then introduce a typical simulation of an overturning rogue wave, and analyze the sensitivity of its geometry and kinematics to water depth and maximum angle of directional energy focusing. We find that an overturning rogue wave can have different properties depending on whether it is in the focusing or defocusing phase at breaking onset. The maximum focusing angle and the water depth largely control this situation, and therefore the main features of the rogue wave crest, such as its 3D shape and kinematics.

1 Introduction

The purpose of this work is to study the rare but important phenomenon of rogue waves at sea (also known as extreme or freak waves). Despite their low probability

of occurrence [35], rogue waves can cause severe damage to vessels or fixed ocean structures. Hence, the naval and offshore engineering communities must be able to predict rogue wave loading on structures, when developing design rules. Earlier work shows that rogue waves are characterized by their brief occurrence in space and time, resulting from a local focusing of wave energy. This energy focusing, in addition to a "natural" occurrence through self-focusing (sideband instability [1,36,52,18], see below), may be due or reinforced by multiple factors, such as an opposing current [43], bottom topography in shallow water [33], frequential [8] and/or directional focusing [6,7]. Other wave-wave interactions or interactions with the atmosphere may also play a role in this phenomenon. Rogue wave generation mechanisms are further discussed in the recent review article by Kharif and Pelinovsky [38].

Two-dimensional (2D) simulations with space-periodic nonlinear models have confirmed that self-focusing of wave energy occurs in irregular wave trains and may cause the occurrence of extreme/rogue waves, after long distance and time of propagation [6,15,52]. Because of its occurrence in small regions of space and time, the latter phenomenon has sometime been referred to as quasi-solitonic turbulence [52]. More recently, mainly due to improvements in accuracy and efficiency of fully nonlinear spectral models, similar space-periodic but three-dimensional (3D) simulations have confirmed the occurrence of extreme 3D waves in irregular sea surfaces, through 3D self-focusing of energy, given enough spatial area and time [15]. Such 3D waves appear to have 2D profiles in their main vertical cross-sections (i.e., that passing through the crest in the wave's main direction of propagation) qualitatively similar to those of 2D focused waves, but also show lateral spreading in the form of a "croissant" shape of rapidly decreasing elevation. These features make these (natural) 3D rogue waves quite similar to waves produced by the so-called type II instability of bi-periodic wave trains [44,51,7].

Independent of their specific generation mechanism, engineering properties of rogue waves, such as geometry and kinematics, are still poorly known. Since current modeling of the natural occurrence of freak waves through 2D or 3D energy self-focusing both requires to model a large region of space and is computationally expensive, extreme waves have usually been produced in both physical and numerical wavetanks by artificially specifying energy focusing towards some small area of the tank. Early 2D studies, both numerical and experimental, used the mechanism of frequency focusing to create rogue waves [8,36]. Due to dispersion, longer and faster waves, that have been generated earlier, catch up with slower and shorter ones, to create extreme waves by superposition. In 3D space periodic models, energy focusing can be achieved by forcing directional components to focus at some location [15]. In physical tanks or Numerical Wave Tanks (NWTs), one can also use the principle of a snake wavemaker to focus directional wave components in some areas of the tank, thus creating extreme, possibly breaking waves [48,49,7]. In fact, more intense and faster directional energy focusing can be achieved in NWTs by using periodic incident waves [7] rather than irregular wavetrains [16]. It appears that, in either case, the large focused waves show very similar features near their crest and, hence,

somewhat locally loses the memory of the physical phenomenon that has caused energy focusing. [Note, this directional energy focusing can be reinforced by also adjusting the frequency of directional components, to compensate for the increased propagation distance of oblique components.]

Accordingly, in this work we generate extreme overturning rogue waves in a NWT, by simulating directional energy focusing of periodic waves, and investigate their properties and sensitivity to governing parameters. As a first approximation, according to linear theory, different wave components with different phases and directions can superimpose over a small region of space and time and produce a much larger wave [11]. To do so in the NWT, a properly programmed snake wavemaker creates the superposition of several directional sinusoidal wave components, towards a target area of the tank. She et al. [48,49] experimentally studied the kinematics of breaking waves this way, using a PIV technique. Grue et al. [32] conducted similar experiments. Brandini [6] and Brandini and Grilli [7] used the same mechanism of directional energy focusing for generating rogue waves in a fully nonlinear 3D-NWT. They clearly showed that nonlinear effects further reinforce the linear superposition process. More recently, Bonnefoy et al. [5] and Ducrozet et al. [15,16] developed a 3D model based on an efficient high-order spectral solution (HOS) of potential flow equations with a free surface, and compared their results with experiments. They also simulated wave generation by a snake wavemaker. Although their method cannot model overturning waves, it can handle many wave components in a large basin, such as random wave fields with wave components propagating as wave packets. Hence, as indicated before, their method can simulate wave focusing events, similar to those occurring in actual sea states. Finally, Fuhrman and Madsen [21] recently solved similar wave focusing problems using a model based on higher-order Boussinesq (BM) equations. They successfully simulated experiments of Johannessen and Swan [37] for the focusing of random wave trains, including values of the horizontal water velocity measured under the focused wave crests.

Here, we follow the earlier numerical work by Brandini and Grilli [7] and simulate intense directional energy focusing of periodic waves in a 3D-NWT, to create extreme overturning waves. Brandini and Grilli modified Grilli et al.'s 3D Fully Nonlinear Potential Flow (FNPF) model [26], based on the Boundary Element Method (BEM), by implementing a snake wavemaker for wave generation as well as a snake absorbing wavemaker to radiate waves out of a NWT [9,27]. Unlike the HOS or BM models, the present NWT does not break down when wave overturning occurs and hence can potentially simulate more intense 3D energy focusing and thus produce larger single rogue waves (note, computations break down upon impact of the breaker jet on the free surface). Additionally, in the present computations, we benefit from recently extended expressions of non-orthogonal tangential derivatives on the free surface [20], which have been shown to make the 3D-NWT solution both more accurate and stable, particularly within the jet of overturning waves [33]. We also use a more efficient spatial solver based on the Fast Multipole Algorithm (FMA) [40,19]. The computational cost of Grilli et al.'s [26] original method,

which grows quadratically with discretization size, was indeed making highly resolved 3D computations rapidly prohibitive. We alleviate this obstacle by using the FMA to accelerate all the matrix-vector products in the spatial solver. This yields a computational cost that grows almost proportionally to the discretization size [19]. Details of the model and its recent improvements are given in the next section. For completeness, we mention the recent 3D-FNPF-BEM model proposed by Hague and Swan [34], that was used to simulate similar directional focusing problems, to create highly nonlinear but non-breaking wave groups.

As far as wave kinematics is concerned, Kjeldsen [39] stressed that larger particle velocities may be associated with overturning waves than with the highest non-breaking waves. Guyenne and Grilli [33] found that this also applies to 3D solitary waves breaking over a sloping ridge, in shallow water. They also showed that the shape and kinematics of the crest and breaker jet of such large 3D overturning waves is mostly independent of the mechanism that has caused breaking. This property was also suggested in earlier studies of 2D deep water breakers [14]. Hence, we expect that this finding also applies to 3D deep water waves, such as overturning rogue waves. [As noted before, we already observe a strong similarity between the vertical profiles of 2D and 3D focused wavetrains.] Accordingly, we do not have to generate these waves by simulating the actual complex mechanisms occurring in irregular ocean waves (such as discussed above), in order to study their properties. Instead, in the applications, we create 3D overturning waves in the middle of a NWT by properly specifying parameters of the snake wavemaker.

While most studies of rogue waves have so far assumed deep water, it has also been shown that these waves can occur for any water depth and, in fact, may even be more frequent in shallow water [39]. Hence, in this study, we consider an arbitrary finite depth, but specify a flat bottom in the NWT in order to further simplify the problem and concentrate on one focusing mechanism only. [Our numerical model can however feature an arbitrary bottom topography and such effects as topographic focusing could be studied in future work.] Hence, we calculate properties of 3D rogue waves at the onset of overturning, such as crest geometry and kinematics, as a function of water depth and energy focusing (or defocusing), represented by the maximum energy focusing angle specified at the wavemaker.

The wave model equations and numerical methods implemented in the NWT are described in Section 2. The most recent numerical improvements of the NWT are also summarized. Numerical experiments and results, together with their physical interpretation, are presented in Section 3.

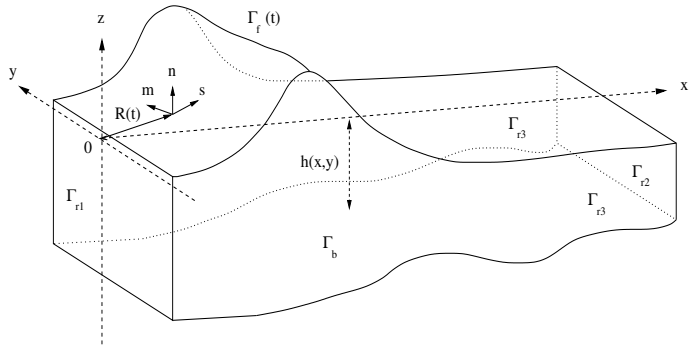

Fig. 1. Computational domain. The free surface $\Gamma_f(t)$ is defined at each time step by the position vector $\boldsymbol{R}(t)$. Lateral boundaries are denoted by Γ_{r1}, Γ_{r2} and Γ_{r3}. The bottom Γ_b is defined by $z = -h(x, y)$. Use is made of the Cartesian coordinate system (x, y, z) and of the local curvilinear coordinate system (s, m, n), defined at the point $\boldsymbol{R}(t)$ of the boundary.

2 The numerical wave tank

2.1 Equations and boundary conditions

We solve potential flow equations for an ideal and incompressible fluid, with a free surface. The velocity $\boldsymbol{u} = (u, v, w)$ is given by $\boldsymbol{\nabla}\phi$, where ϕ is the velocity potential. The computational domain is defined as a closed basin, such as a wave tank, whose bottom may have arbitrary geometry, and lateral boundaries are either impermeable or open (Fig. 1). The governing equation, representing mass conservation within the basin, is Laplace's equation,

$$\nabla^2\phi(x, y, z, t) = 0, \tag{1}$$

for the potential. Green's second identity transforms this equation into the Boundary Integral Equation (BIE),

$$\alpha(\boldsymbol{x}_l)\,\phi(\boldsymbol{x}_l) = \int_{\Gamma(t)} \left\{ \frac{\partial\phi}{\partial n}(\boldsymbol{x})\, G(\boldsymbol{x}, \boldsymbol{x}_l) - \phi(\boldsymbol{x})\, \frac{\partial G}{\partial n}(\boldsymbol{x}, \boldsymbol{x}_l) \right\} \mathrm{d}\Gamma, \tag{2}$$

where $G(\boldsymbol{x}, \boldsymbol{x}_l) = 1/4\pi|\boldsymbol{r}|$ is the 3D free space Green's function in which $\boldsymbol{r} = \boldsymbol{x} - \boldsymbol{x}_l$. The vector $\boldsymbol{n}$ is the normal vector exterior to the boundary, $\alpha(\boldsymbol{x}_l)$ is proportional to the exterior solid angle of the boundary at point $\boldsymbol{x}_l$, and Γ denotes the entire domain boundary.

On the free surface boundary $\Gamma_f(t)$, the potential satisfies the nonlinear kinematic and dynamic boundary conditions,

$$\frac{D\,\boldsymbol{R}}{D\,t} = \boldsymbol{\nabla}\phi, \tag{3}$$

$$\frac{D\,\phi}{D\,t} = -gz + \frac{1}{2}\,\boldsymbol{\nabla}\phi\cdot\boldsymbol{\nabla}\phi, \tag{4}$$

where $\boldsymbol{R}$ is the position vector on the free surface, g the acceleration due to gravity and D/Dt the material derivative. [Note that surface tension is omitted here since we are interested in gravity waves with a wavelength large enough to avoid a significative influence of surface tension on wave breaking (see for instance [17]).]

Lateral boundaries of the domain are either fixed or moving boundaries. Here, waves are generated by a wavemaker with motion $\boldsymbol{x}_p$ and velocity $\boldsymbol{u}_p$, specified at boundary $\Gamma_{r1}(t)$. Hence, the boundary condition on Γ_{r1} reads

$$\overline{\boldsymbol{x}} = \boldsymbol{x}_p \quad \text{and} \quad \overline{\frac{\partial\phi}{\partial n}} = \boldsymbol{u}_p\cdot\boldsymbol{n}, \tag{5}$$

where overbars denote specified values. Along fixed impermeable parts of the boundary, Γ_{r3}, a no-flow condition is prescribed as

$$\overline{\frac{\partial\phi}{\partial n}} = 0. \tag{6}$$

For flat bottoms, like in this work, the image method is used to automatically satisfy a no-flow condition similar to Eq. (6) along the bottom boundary Γ_b. For wave focusing experiments, in order to simulate an open boundary condition, an actively absorbing, pressure sensitive, snake piston wavemaker is specified at the extremity $\Gamma_{r2}(t)$ of the NWT [9,27]. The piston normal velocity is specified as

$$\overline{\frac{\partial\phi}{\partial n}} = u_{ap}(x_p, y_p, t) \tag{7}$$

with the latter calculated at point (x_p, y_p) along the piston as

$$u_{ap}(x_p, y_p, t) = \frac{1}{\rho_w d\sqrt{gd}} \int_{-d}^{\eta_{ap}(x_p,y_p,t)} p_D(x_p, y_p, z, t)\,dz. \tag{8}$$

Here ρ_w is the water density, d the mean water depth, η_{ap} the surface elevation at the piston, and $p_D = -\rho_w(\phi_t + \frac{1}{2}\boldsymbol{\nabla}\phi\cdot\boldsymbol{\nabla}\phi)$ the dynamic pressure. The integral in Eq. (8) represents the horizontal hydrodynamic force $F_D(x_p, y_p, t)$ acting on the piston at time t, as a function of (x_p, y_p). [A validation of this snake absorbing boundary condition for solitary waves can be found in [31].]

With a BIE formulation, the numerical solution can be explicitly calculated inside the domain based on boundary values. For instance, the vectors $\boldsymbol{u}$ for the internal velocity and $\boldsymbol{a}$ for the local acceleration are given respectively by

$$\boldsymbol{u}(\boldsymbol{x}_l) = \boldsymbol{\nabla}\,\phi(\boldsymbol{x}_l) = \int\limits_{\Gamma(t)} \left\{ \frac{\partial \phi}{\partial n}(\boldsymbol{x})\, Q(\boldsymbol{x}, \boldsymbol{x}_l) - \phi(\boldsymbol{x})\, \frac{\partial Q}{\partial n}(\boldsymbol{x}, \boldsymbol{x}_l) \right\} \mathrm{d}\Gamma, \tag{9}$$

$$\boldsymbol{a}(\boldsymbol{x}_l) = \boldsymbol{\nabla}\,\frac{\partial \phi}{\partial t}(\boldsymbol{x}_l) = \int\limits_{\Gamma(t)} \left\{ \frac{\partial^2 \phi}{\partial t \partial n}(\boldsymbol{x})\, Q(\boldsymbol{x}, \boldsymbol{x}_l) - \frac{\partial \phi}{\partial t}(\boldsymbol{x})\, \frac{\partial Q}{\partial n}(\boldsymbol{x}, \boldsymbol{x}_l) \right\} \mathrm{d}\Gamma, \tag{10}$$

with

$$Q(\boldsymbol{x}, \boldsymbol{x}_l) = \frac{1}{4\pi |\boldsymbol{r}|^3} \boldsymbol{r}, \tag{11}$$

and

$$\frac{\partial Q}{\partial n}(\boldsymbol{x}, \boldsymbol{x}_l) = \frac{1}{4\pi |\boldsymbol{r}|^3} \{ \boldsymbol{n} - 3(\boldsymbol{e_r} \cdot \boldsymbol{n}) \boldsymbol{e_r} \}, \quad \text{with } \boldsymbol{e_r} = \boldsymbol{r}/|\boldsymbol{r}|. \tag{12}$$

The internal Lagrangian acceleration can then be obtained from

$$\frac{D\,\boldsymbol{u}}{D\,t} = \frac{D\,\boldsymbol{\nabla}\phi}{D\,t} = \frac{\partial \boldsymbol{\nabla}\phi}{\partial t} + (\boldsymbol{\nabla}\phi \cdot \boldsymbol{\nabla}) \boldsymbol{\nabla}\phi. \tag{13}$$

Indeed, the first term is given by (10) and the second term is computed using (9) and differentiating $\boldsymbol{\nabla}\phi$, which requires the evaluation of a BIE similar to (9), using instead the spatial derivatives of Q and $\partial Q/\partial n$ [33].

2.2 Numerical techniques

Many different numerical methods have been proposed for solving FNPF equations for water waves (see, e.g., [13] for a recent review). Here, we use the BIE formulation outlined above, which was applied to our original 3D-NWT by Grilli et al. [26], with recent improvements in the numerical formulation and solution [20,19]. A brief summary is given below.

The time stepping algorithm consists of updating the position vector and velocity potential on the free surface, based on second-order Taylor series expansions. At each time step, the BIE (2) is expressed for N nodes defining the domain boundary, and solved with a BEM. Thus, elements are specified in between nodes, to locally

interpolate both the boundary geometry and field variables, using bi-cubic polynomial shape functions. A local change of variables is defined to express the BIE integrals on a curvilinear reference element, and compute these using a Gauss-Legendre quadrature and other appropriate techniques removing the weak singularities of the Green's function (based on polar coordinate transformations). The number of discretization nodes yields the assembling phase of the system matrix, resulting in an algebraic system of equations. The rigid mode technique is applied to directly compute angles α and diagonal terms in the system, which normally requires evaluating strongly singular integrals involving the normal derivative of the Green's function. This modifies the algebraic system as well. Multiple nodes are specified on domain edges and corners, in order to easily express different normal directions on different sides of the boundary. Additional equations derived for enforcing continuity of the potential at these nodes also lead to modifications of the algebraic system matrix. The velocity potential (or its normal derivative depending on the boundary condition) is obtained as a solution of the linear system of equations. Since the system matrix is typically fully populated and non-symmetric, the method has, at best, a computational complexity of $O(N^2)$, when using the iterative, optimized conjugate gradient method GMRES. Thus the spatial solution at each time step is of the same complexity as the assembling of the system matrix. The Fast Multipole Algorithm (FMA) is implemented to reduce this complexity.

First developed by Greengard and Rokhlin [24] for the N-body problem, the FMA allows for a faster computation of all pairwise interactions in a system of N particles, in particular, interactions governed by Laplace's equation. Hence, it is well suited to our problem. The basis of the algorithm is that the interaction strength decreases with distance, so that points that are far away on the boundary can be grouped together to contribute to one collocation point. A hierarchical subdivision of space automatically verifies distance criteria and distinguishes near interactions from far ones. The FMA can be directly used to solve Laplace's equation, but it can also be combined with an integral representation of this equation. The discretization then leads to a linear system, with matrix-vector products evaluated as part of an iterative solver (such as GMRES), that can be accelerated using the FMA. Rokhlin [46] applied this idea to the equations of potential theory. A review of the application of this algorithm to BIE methods can be found in [45]. Korsmeyer et al. [40] combined the FMA with a BEM, through a Krylov-subspace iterative algorithm, for water wave computations. Following Rokhlin's ideas, they designed a modified multipole algorithm for the equations of potential theory. First developed for electrostatic analysis, their code was generalized to become a fast Laplace solver, which subsequently has been used for potential fluid flows. Their model was efficient but its global accuracy was limited by the use of low order boundary elements. Scorpio and Beck [47] studied wave forces on bodies with a multipole-accelerated desingularized method, and thus did not use boundary elements to discretize the problem. Neither did Graziani and Landrini [22], who used the Euler-McLaurin quadrature formula in their 2D model. Srisupattarawanit et al. [50] also used a fast multipole solver to study waves coupled with elastic structures. We show briefly

below how the FMA can be combined with Grilli et al.'s [26] 3D-NWT to yield a more efficient numerical tool. Details can be found in [19].

The FMA is based on the principle that the Green's function can be expanded in a series of separated variables, for which only a few terms need to be retained, when the source point $\boldsymbol{x}_l$ and the evaluation point $\boldsymbol{x}$ are far enough from one another. Thus, for a point $\boldsymbol{O}$ (origin of the expansion) close to $\boldsymbol{x}$ and far from $\boldsymbol{x}_l$, we have,

$$G(\boldsymbol{x}, \boldsymbol{x}_l) \approx \frac{1}{4\pi} \sum_{k=0}^{p} \sum_{m=-k}^{k} \rho^k Y_k^{-m}(\alpha, \beta) \frac{Y_k^m(\theta, \varphi)}{r^{k+1}}, \tag{14}$$

where $\boldsymbol{x}-\boldsymbol{O} = (\rho, \alpha, \beta)$ and $\boldsymbol{x}_l-\boldsymbol{O} = (r, \theta, \varphi)$ in spherical coordinates. The functions $Y_k^{\pm m}$ are the spherical harmonics defined from Legendre polynomials. A hierarchical subdivision of the domain, with regular partitioning automatically verifying distance criteria, is defined to determine for which nodes this approximation applies. Thus, close interactions are evaluated by direct computation of the full Green's functions, whereas far interactions are approximated by successive local operations based on the subdivision into cells and the expansion of the Green's function into spherical harmonics. The underlying theory for this approximation is well established in the case of Laplace's equation. In particular, error and complexity analyses are given in the monograph by Greengard [23].

In our case, Laplace's equation has been transformed into a BIE and a specific discretization has been used. Thus, the FMA must be adapted in order to be part of the surface wave model, but the series expansion (14) remains the same. Hence, with the FMA, Eq. (2) can be rewritten as

$$\alpha(\boldsymbol{x}_l)\, \phi(\boldsymbol{x}_l) \approx \frac{1}{4\pi} \sum_{k=0}^{p} \sum_{m=-k}^{k} M_k^m(\boldsymbol{O}) \frac{Y_k^m(\theta, \varphi)}{r^{k+1}}, \tag{15}$$

where moments $M_k^m(\boldsymbol{O})$ are defined as

$$M_k^m(\boldsymbol{O}) = \int_\Gamma \left\{ \frac{\partial \phi}{\partial n}(\boldsymbol{x})\, \rho^k Y_k^{-m}(\alpha, \beta) - \phi(\boldsymbol{x})\, \frac{\partial}{\partial n}\Big(\rho^k Y_k^{-m}(\alpha, \beta)\Big) \right\} \mathrm{d}\Gamma. \tag{16}$$

Instead of considering mutual interactions between two points on the boundary, we now need to look at the contribution of an element of the discretization to a collocation point. The local computation of several elements, grouped together into a multipole, relies on a BEM analysis using the spherical harmonic functions instead of the Green's function. The integration of the normal derivative of the spherical harmonics is done by taking care of avoiding an apparent singularity, which could generate numerical errors. The BEM discretization only applies to the computation of the moments. Thus, the rest of the FMA is unchanged, especially regarding

translation and conversion formulae, which allow to pass the information through the hierarchical spatial subdivision, from the multipole contributions to the matrix evaluation for each collocation node. In the 3D-NWT, the use of the FMA only affected parts that involved the assembling and the solution of the algebraic system matrix. The storage of coefficients that are used several times for each time step, for instance, is now done inside the cells of the hierarchical subdivision. The rigid mode and multiple nodes techniques, which *a priori* modified the matrix before the computation of matrix-vector products, are now considered as terms correcting the result of such products, so that the linear system keeps the same properties.

The accelerated model benefits from the faster Laplace's equation solver at each time step. The FMA model performance was tested by comparing new results with results of the former model, for a 3D application which requires great accuracy : the propagation of a solitary wave on a sloping bottom with a transverse modulation, leading to a plunging jet [26]. The consistency of the new solution was checked but, more importantly, the accuracy and stability of results and their convergence as a function of discretization size was verified. In fact, by adjusting the parameters of the FMA, i.e. the hierarchical spatial subdivision and the number of terms p in the multipole expansions, one can essentially obtain the same results as with the former model. In this validation application, for discretizations having more than 4,000 nodes, the computational time was observed to increase nearly linearly with the number of nodes [19].

The present applications have a horizontal symmetry and a flat bottom in the computational domain. Hence, the image method can be applied with respect to the planes $z = -d$ and $y = 0$, to remove parts of the discretization [7]. Doing so, the 3D free space Green's function is modified in the BIE, by adding contributions of each image source. In the FMA, when the original source point is far from the collocation point, so are the images. Thus, image contributions have simply been added to the multipole associated with the original point. In the usual application of the FMA, images should be accounted for at a coarser subdivision level than the original source points, since they are further away from the evaluation point.

3 Numerical experiments

3.1 Introduction

We generate extreme waves in a 3D-NWT by directional energy focusing, up to overturning, i.e. the first stage of breaking. The large size of the extreme waves we are modeling justifies neglecting capillary and viscous effects. In the absence of surface tension and viscosity, wave breaking is initiated by an overturning motion at the tip of the wave crest [17]. For such cases, the potential flow solution has been

shown to be in good agreement with experiments [14,28–30]. We do not attempt to model the subsequent turbulent part of breaking, with air entrainment and bubbles. Potential flow would no longer apply and other models would be required to this effect, for instance, a VOF-Navier-Stokes solver coupled to the BEM model [41,2,3,10] or directly applied [42] to the simulation. Moreover, for the same reason, we focus our interest on plunging breakers, for which there is a clean large size jet, rather than the more turbulent spilling breakers.

We generate an extreme overturning wave in the 3D-NWT, by simple geometrical focusing, using a snake wavemaker. Since our goal is to study wave kinematics we do not try to reproduce a prespecified target wave, as e.g. in [37,5], but rather we produce as large a breaker as possible, given the specified water depth. Besides, our selected wave generation method creates evanescent modes, free waves, and nonlinear interactions, which would not easily be taken into account, when attempting to generate a specific target wave through inverse modeling. Such an iterative adjustment of generation parameters might be necessary for performing physical wavetank experiments, in which various gages must be strategically located, but is less crucial in numerical experiments, where results are available everywhere.

We only present idealized situations of extreme wave generation, in order to show the dependence of wave properties on governing parameters, such as the maximum wave focusing angle and water depth. Thus, only a moderate number of periodic wave components are specified at the wavemaker, which all geometrically focus at one point in the NWT, according to the linear approximation. Large, perhaps not fully realistic, values of maximum angular directionality are typically used, to produce the wave focusing event not too far from the wavemaker, and hence reduce the length of the computational domain. In light of the present simulation results, future work will deal with the generation of more realistic extreme waves, from a directional wave spectrum. Such cases will involve longer and more expensive computations, requiring the implementation of a more efficient open boundary condition in the 3D-NWT in order to minimize reflection [27,9].

3.2 Wave focusing

For the idealized applications considered in this paper, the NWT is defined as a rectangular basin with a flat bottom at depth $z = -d$ (Fig. 1). Laterally, the NWT is bounded by fixed or moving, initially vertical, boundaries. A snake wavemaker is specified on the $x = 0$ side of the tank, consisting of multiple flap paddles rotating on the bottom, with the angular velocity $\dot{\omega}\,\boldsymbol{j}$ [7] and horizontal stroke $S_o(y,t)$ at $z = 0$. Each wavemaker paddle thus has an angle $\omega = \arctan S_o/d$ and a position $\boldsymbol{x}_p = (x_p, y_p, z_p)$ defined by

$$\boldsymbol{x}_p = \boldsymbol{x}_o - \rho\,\boldsymbol{m}, \tag{17}$$

with $\boldsymbol{x}_o = y_p\,\boldsymbol{j} - d\,\boldsymbol{k}$ the coordinates of the axis of rotation of the paddle, and $\rho = \sqrt{x_p^2 + (d+z_p)^2}$ the distance from points on the wavemaker to this axis.

¿From these definitions, we find the velocity and acceleration vectors on the wavemaker as

$$\begin{aligned} \boldsymbol{u}_p &= -\dot{\rho}\,\boldsymbol{m} - \rho\,\dot{\omega}\,\boldsymbol{n} \\ \frac{\mathrm{d}\boldsymbol{u}_p}{\mathrm{d}t} &= (\rho\,\dot{\omega}^2 - \ddot{\rho})\,\boldsymbol{m} - (2\,\dot{\rho}\,\dot{\omega} + \rho\,\ddot{\omega})\,\boldsymbol{n}. \end{aligned} \tag{18}$$

The snake wavemaker stroke function is defined, according to linear theory [11], as a linear superposition of N_θ sinusoidal components of amplitude a_n and direction θ_n. Angles θ_n are uniformly distributed in the range $[-\theta_{\max}, \theta_{\max}]$. We find

$$S_o(y,t) = \sum_{n=1}^{N_\theta} a_n \cos\{k_n(y\sin\theta_n - x_f\cos\theta_n) - \Omega_n t\}, \tag{19}$$

where x_f is a geometrical focusing distance for the waves in front of the wavemaker, and k_n and Ω_n denote the wavenumber and frequency of each component, respectively, satisfying the linear dispersion relationship

$$\Omega_n^2 = g\,k_n\,\tanh(k_n d). \tag{20}$$

Based on linear wavemaker theory, each wave component amplitude can be estimated as [12]

$$A_n = a_n \frac{1}{cos(\theta_n)} \frac{4\sinh(k_n d)(1-\cosh(k_n d) + k_n d\sinh(k_n d))}{k_n d(2k_n d + \sinh(2k_n d))}, \tag{21}$$

and at the linearly defined focal point $x = x_f$, the total amplitude is estimated by $A^* = \sum A_n$.

In order to reduce initial singularities at the interface between the free surface and the moving wavemaker, the wavemaker is gradually set in motion in the computations, following a tanh-like ramp-up over three representative wave periods [7].

The above describes the simplest way of generating wave focusing with a snake wavemaker, and Fig. 2 shows an example of snake wavemaker motion. More complex motions could be achieved. In particular, only directional focusing is used in all the cases reported here, and hence $\Omega_n = \Omega$. Frequency focusing can be specified by adjusting the frequency (or celerity) of wave components as a function of θ_n so that they (linearly) reach the focal point at the same time. Given the celerity c_o of the

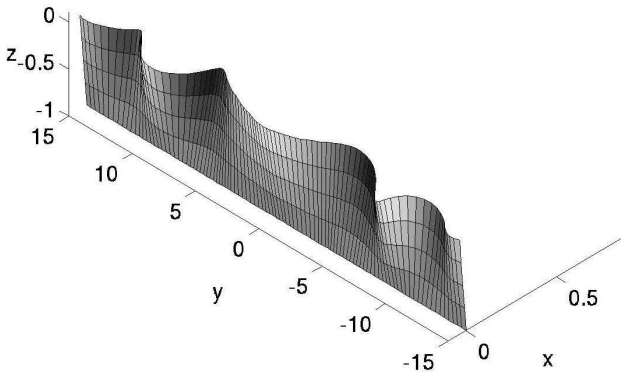

Fig. 2. Illustration of the snake motion of the wavemaker located at the left of the tank. Data used corresponds to one of the cases described in the following.

normal component corresponding to $\theta_n = 0$, the celerity for oblique components is $c_n = \Omega_n/k_n = c_o/\cos\theta_n$. Moreover, for simplicity, we assume that the amplitudes of the wavemaker components are all identical ($a_n = a$). Different values could be selected in order to model a real sea state with a specified energy spectrum. Finally, as mentioned above, even with this simplest case, the wavemaker generates a more complex wave field than predicted by linear wave theory, due to both the finite size of the wavetank and nonlinear effects. This leads to changes in focal point locations and maximum wave height. Perfect focusing, however, is not the topic of the present study, and this wavemaker law of motion serves our purpose well enough.

In the following, we give results of two wave focusing applications. The first one details a single wave focusing case and discusses features of the plunging breaker that is generated. The second one presents a comparison of focusing results obtained for nine cases, with different water depth and directionality parameters. All computations were performed with non-dimensionalized equations, obtained by dividing lengths by the water depth d of our first case, and times by $\sqrt{d/g}$. Therefore, all results in the figures are also given in this non-dimensionalized form. In order to give an idea for actual physical values, results in the text are given with a characteristic depth of 20 m (corresponding roughly to coastal waters in the North Sea [38]).

3.3 Analysis of an overturning rogue wave

First we consider the superposition of $N_\theta = 30$ wave components having identical properties, but with directions varying between $-\theta_{\max} = -45$ and $\theta_{\max} = 45$ degrees. Each component has a frequency $\Omega = 0.8971$ rad/s, for which Eq. (20) gives a (linear) wavelength $L = 2\pi/k = 72$ m, a period $T = 7$ s, and a linear celerity $c = \Omega/k = 10.28$ m/s, all for a water depth of $d = 20$ m. The amplitude of each individual wavemaker stroke component is fixed to $a = 0.2$ m, yielding an individual wave amplitude of $A = 0.19$ m for a (linear) steepness of $kA = 0.0162$ (for the wave component propagating at the angle $\theta_n = 0$). The amplitude at the

linear focal point, specified at the distance $x_f = 250$ m from the wavemaker, is thus theoretically $A^* = 6.3$ m. This is clearly a large value, in accordance with our goal of generating a large overturning wave early in the generation process, before reaching the far end of the tank where, despite the absorbing boundary condition, some reflection occurs that may perturb wave focusing.

The NWT has a 440 m length (or $22d$) and a 600 m width (or $30d$). For the selected focusing distance, this NWT length is such that, when overturning of the extreme wave occurs, almost no wave will have yet reached the far end of the tank. Hence, the absorbing boundary condition will not be activated in this computation. The width of the NWT along y is divided into 70 elements, and its depth into 4 elements. At the beginning of computations, the discretization has 90 elements in the $x-$longitudinal direction, which corresponds to roughly 15 nodes per wavelength. In order to better resolve the wave steepening towards breaking (defined as the occurrence of the first vertical tangent on the free surface), the resolution is later improved by using 120 elements with an irregular grid, refined around the breaking wave for $t > 43.39$ s ($= 6.20T$). The present simulations require 2 min per time step on a biprocessor Xeon (3Ghz, 2Go RAM) for the initial grid, and 10 min 30 s per time step for the finer one.

Figure 3 shows the time evolution of the non-dimensional surface wave field. The initially flat free surface starts moving near the wavemaker (Fig. 3a) and, due to the ramp-up motion, a first focused wave of moderate amplitude is generated (Fig. 3b). Then, this wave elevation decreases (not shown) and almost disappears at the plot scale. Hence, our focusing mechanism effectively produces local focusing that is transient both in time and space. The amplitude of the wavemaker oscillations further increases to give rise, in Fig. 3c, to an even larger wave in the middle of the tank and, eventually, after the transient ramp-up of the wavemaker motion is over and complete focusing is achieved, to an even larger wave that starts overturning around $x_c = 211$ m (or 10.55 d) (Fig. 3d). This is closer to the wavemaker than the linearly estimated focal point. Behind this breaker, we see on the figure that the phenomenon is starting to repeat itself, with a new curved crest line appearing and converging towards the center of the NWT.

The observation of the free surface shape at focusing for this 3D application leads to the following additional comments. First of all, there is a circular trough located just in front of the overturning wave (the so-called "hole in the sea" reported by rogue wave eyewitnesses). Behind the wave, an even deeper trough has formed (which is more clearly seen in Fig. 4), separating the main wave from the curved crest line which follows it. This trough has more of a crescent shape, due to the directions of the incoming waves. The overturning wave itself appears like a curved front as well. In the present case, for which directionality is significant, the front is not so wide, reflecting strong 3D effects. The amplitude of the overturning wave is significantly larger than that of the following waves, which have not yet converged, and the wave has a strong back-to-front asymmetry (this is also more clearly seen on Fig. 4).

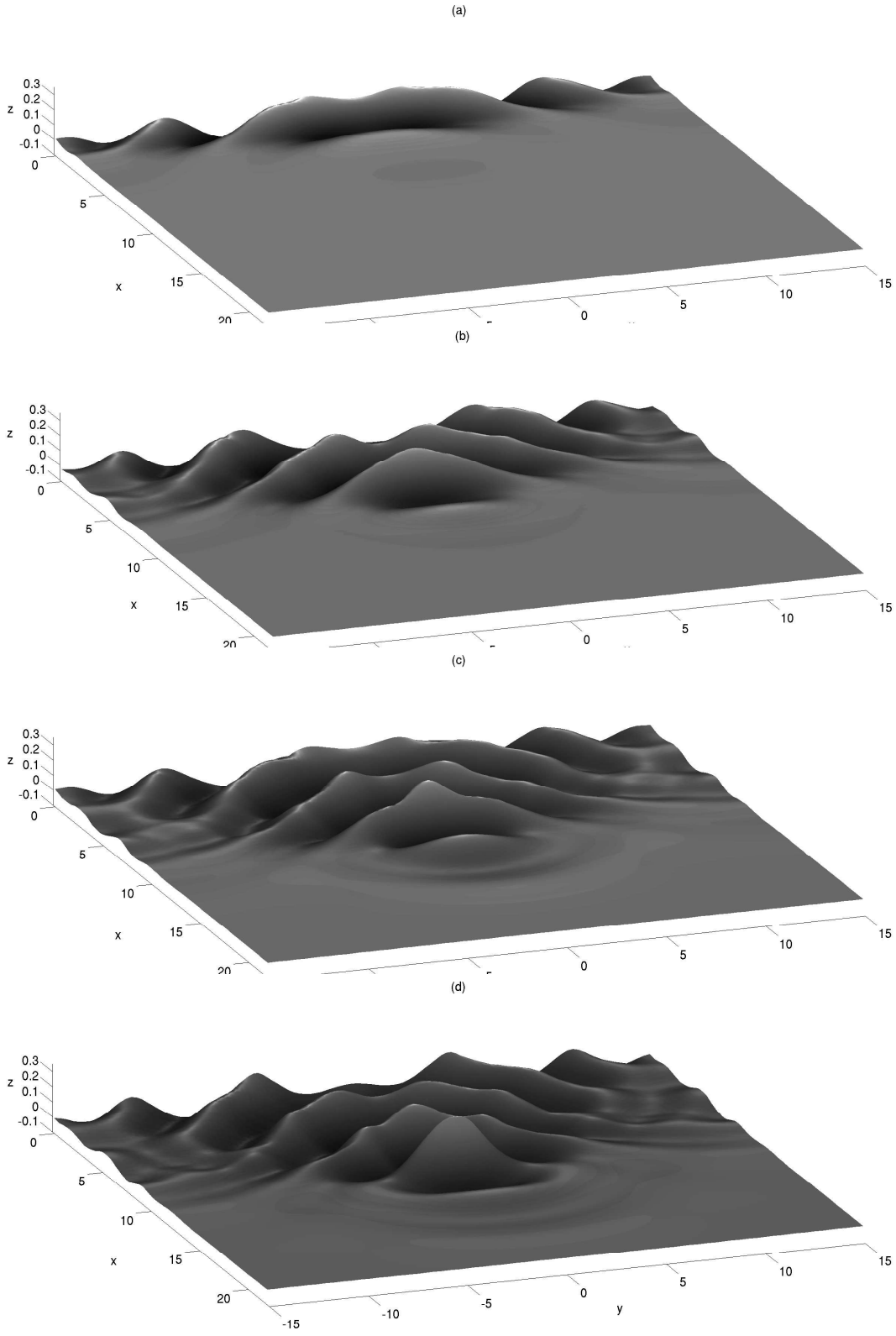

Fig. 3. Free surface evolution at : (a) $t = 3.11T$, (b) $t = 4.74T$, (c) $t = 6.20T$, (d) $t = 6.89T$. In the last figure, the focused wave is starting to overturn, with its crest located at $x = 211$ m (or 10.55 d).

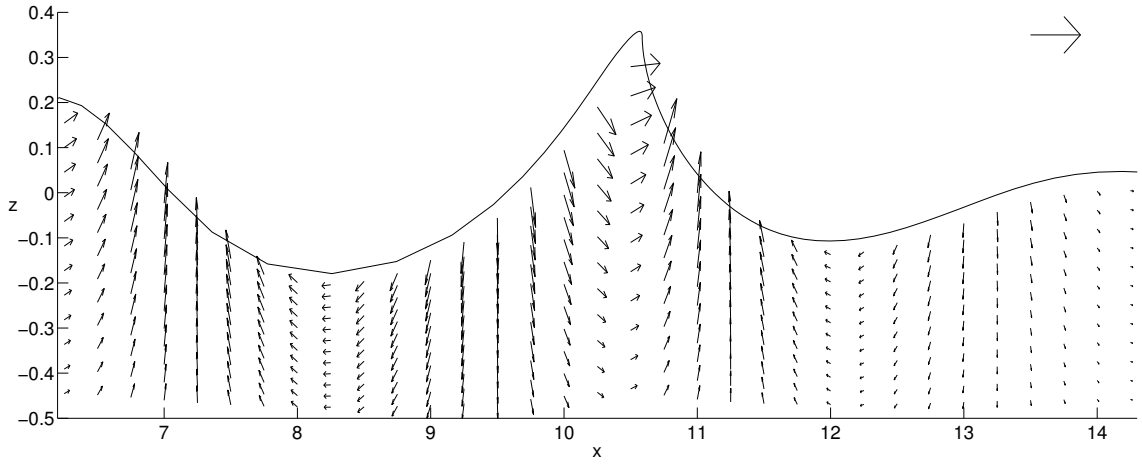

Fig. 4. Vertical slice at $y = 0$ and $t = 6.89T$ in Fig. 3d. The arrows show the projected velocity vectors. The arrow in the upper-right corner represents the unit vector. The vertical axis is exaggerated by a factor 9.

This wave asymmetry increases with time, prior to reaching the breaker point, and indicates that the wave is about to overturn and break.

The dominant nonlinear effect in this application is clearly the wave steepening towards breaking. In particular, this application was not designed to study the transfer of energy inside an incoming wave group, as in studies related to modulational instability leading to the sudden appearance of a very large wave. Here, the wave starts to break before the focusing mechanism can fully develop and possibly lead to an even bigger wave; however our numerical method is limited as it cannot continue computations beyond breaking.

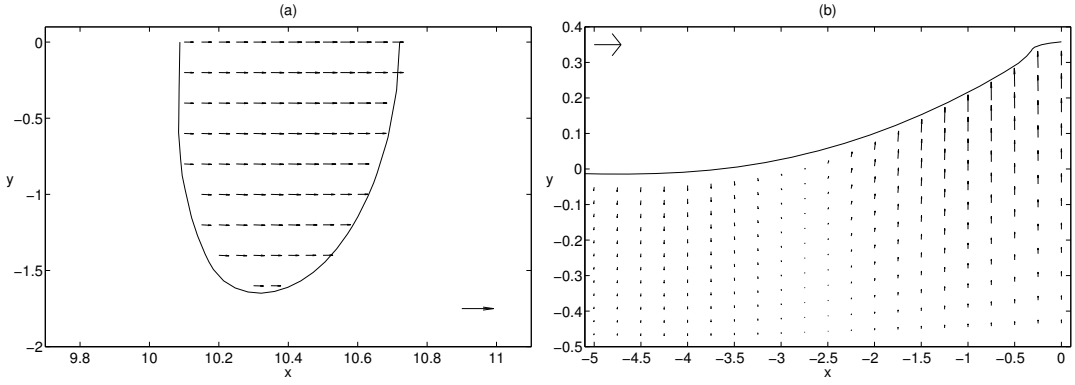

Fig. 5. Horizontal cross-section at $z = A_c/2$ (left) and transverse vertical cross-section at $x = x_c$ and $t = 6.89T$, in Fig. 3d. The arrows show the projected velocity vectors.

The properties of the extreme wave generated in this application agree well with known characteristics of rogue waves, and more generally of transient breaking waves. In particular, the vertical cross-section at $y = 0$ and $t = 6.89T = 48.23$ s in Fig. 3d, given in Fig. 4, shows that the wave profile is similar to that observed in rogue wave measurements or observations (see for example the extreme wave

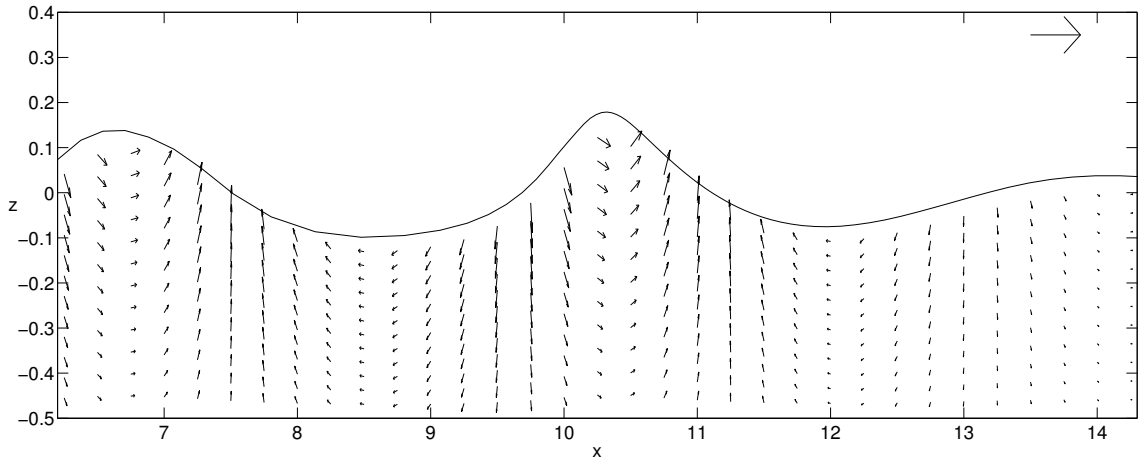

Fig. 6. Vertical slice at $y = \pm\ell/2 = 36$ m and $t = 6.89T$, in Fig. 3d. The arrows show the projected velocity vectors. The vertical axis is exaggerated by a factor 5.8.

measured under the Draupner platform in the North Sea on January 1st 1995), as well as in earlier 2D numerical studies, for instance those related to modulational instabilities of a wave packet [38]. A large crest ($A_c = 7.16$ m or $0.358d$) is preceeded and followed by two much shallower troughs; the back trough is deeper than the front one ($A_{t1} = 3.60$ m and $A_{t2} = 2.14$ m, or $0.180d$ and $0.107d$, respectively). Wave height is $H_1 = A_c + A_{t1} = 10.76$ m or $0.538d$, which is less than the linearly predicted upper bound value $2A^* = 12.6$ m. As discussed above, this is because of the early breaking of the wave, and the incomplete focusing. Also, since no frequency focusing was specified, not all waves lead to constructive interferences at the focal point, even in a linear sense. The wavelength of the nonlinear focused wave can also be measured on Fig. 4, by averaging the rear and front wavelengths (i.e., mean water level distance between two zero-crossing points) using the back and the front trough. We find $\lambda \simeq 78.0$ m (or 3.90 d), which is more than the linear value, due to amplitude dispersion effects [12]. This yields a steepness $H/\lambda = 0.138$, which is greater than the limiting steepness predicted by Miche's law for this depth, about 0.132 (for a symmetric maximum Stokes wave [12]). Hence, the asymmetric and transient extreme wave generated in the NWT in this application grows further than the theoretical limiting steepness, before it overturns. This may have important implications for structural design of offshore structures [10].

Figures 5–6 illustrate the 3D shape of the focused wave. [Note that contours shown in these figures are less smooth than the actual wave surface, because of the interpolation algorithm.] In the horizontal slice at height $z = A_c/2$ (Fig. 5a), we see an elliptic-shaped contour of the surface elevation (only one-half is shown since the problem is symmetrical with respect to the (x, z)-plane). However a pronounced asymmetry is visible between the back and the front of the wave, as expected from the 2D wave profile shown in Fig. 4, corresponding to a more curved front face than the back face of the wave, which is rather straight. The vertical lateral cross-section at $x = x_c$ is shown in Fig. 5b. The transverse shape of the wave is quite triangular,

so that the 3D wave is approximately pyramidal. This could be due to the large value of θ_{max}, which creates intense focusing over a small area and hence concentrates well wave energy. [Note that the development of a large breaker that follows this stage will tend to give the wave a more rounded transverse shape.] To further confirm the 3D nature of the focused wave, we show in Fig. 6 a vertical cross-section taken at $y = \pm\ell/2 = 36$ m, where ℓ is the wave width at mid-height. We observe here that, for this smaller wave elevation, the back-to-front asymmetry is almost non-existant, while the crest-to-trough asymmetry is very pronounced, indicating significant wave nonlinearity.

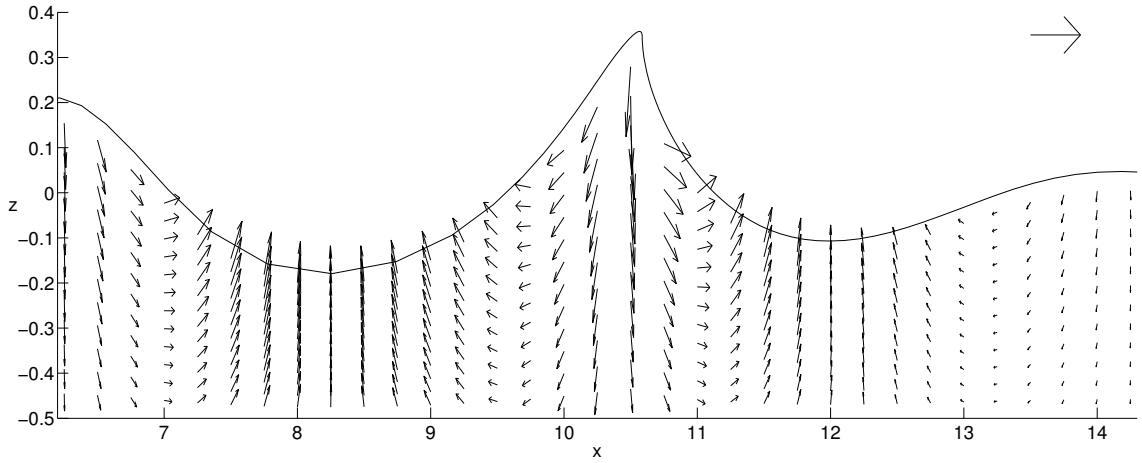

Fig. 7. Same parameters as Fig. 4. The arrows show the projected internal accelerations vectors. The arrow in the right-hand corner represents the unit vector.

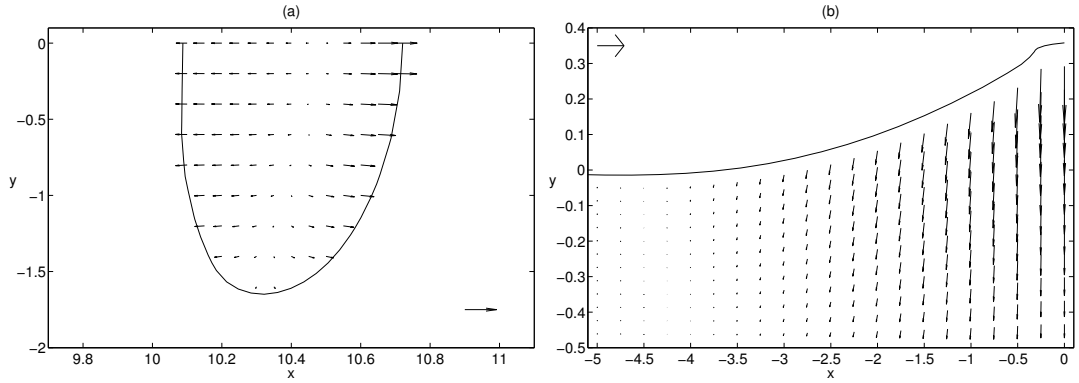

Fig. 8. Same parameters as Fig. 5. The arrows show the projected internal accelerations vectors.

Besides wave shapes, Figs. 4 to 6 show projections of internal velocity vectors on each cross-section. Figs. 7 to 9 present similar projections for the internal acceleration vectors at the same cross-sections. Figs. 4 and 7 illustrate the more intense kinematics at incipient breaking immediately below the wave crest. The horizontal cross-section in Fig. 5a shows that the horizontal velocity field is nearly (laterally) uniform at mid-height. For the corresponding acceleration field in Fig. 8a, we see positive accelerations (of magnitude $\approx g$) in the front tier zone, and negative values

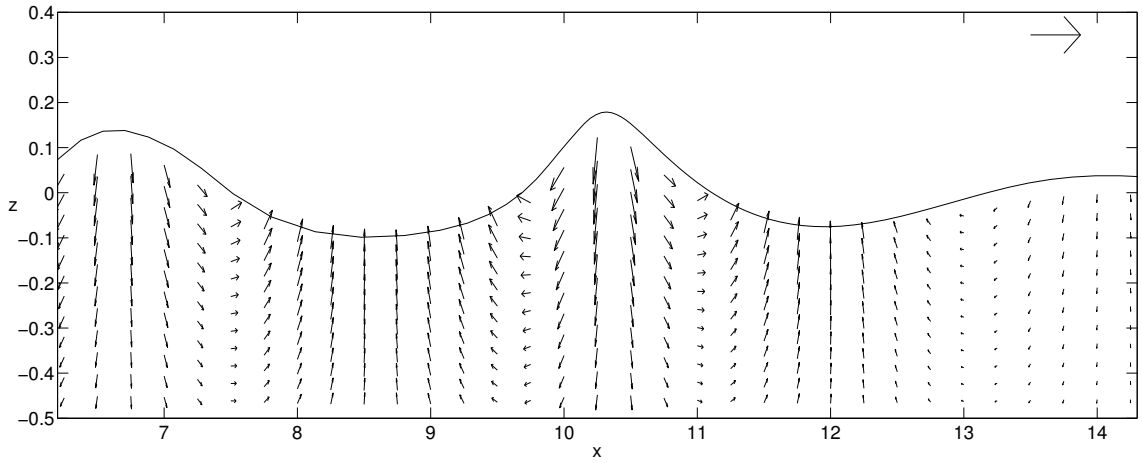

Fig. 9. Same parameters as Fig. 6. The arrows show the projected internal accelerations vectors.

in the back. We note that the transverse effects seem rather small at this level. This is confirmed by the transverse vertical cross-sections of Figs. 5b and 8b. Particle velocities are essentially upwards, with the upper part of the fields having nearly uniform values. Accelerations are negative, with greater values ($\simeq 2g$) nearest the crest. Finally, the flow in the section at $y = \pm\ell/2$ does not show particular features, other than those of a typical periodic nonlinear wave, the crest having not yet started overturning (Figs. 6 and 9).

Velocity and acceleration fields (not shown) computed on the free surface for the same stages as shown in Fig. 3 show two main phases in the evolution of the focused wave event. The first phase is one of approach, in which the different wave components forming a crest line are converging towards the focal point. Wave kinematics thus shows features similar to the propagation of a curved crest line. The second phase corresponds to the appearance of a unique, large, focused wave, resulting from the superposition of many components. This stage is shown in Fig. 10 at the time of breaking, corresponding to Fig. 3d. Upon focusing, the maximum value of the longitudinal velocity component u increases, and the largest velocities concentrate more and more towards the wave crest, indicating flow convergence. At the same time, as we have seen, the decreasing transverse components of the velocity and acceleration fields in the upper half of the focused wave crest, notably smaller than for the wave that follows, indicate that the flow becomes more and more 2D (in y-planes). The focused wave crest tends to move forward faster than the phase velocity of its basic wave components, thus initiating overturning and breaking. This is in agreement with internal field patterns discussed above. Hence, the dynamics of a rogue wave which is about to break becomes almost 2D locally. [This observation has important implications for the design of offshore structures that would be located in the path of such a wave [10].] This is in good agreement with descriptions of a "wall of water", reported in stories relating extreme wave events in the ocean.

Accelerations are not shown on the free surface, because these are in part calculated

by differentiation and hence become less accurate near the crest of the focused wave, due to the very deformed free-surface geometry. However internal fields presented above, which are calculated with the BIEs (Figures 7 to 9), are much more accurate, particularly when they are computed not too close to the free surface.

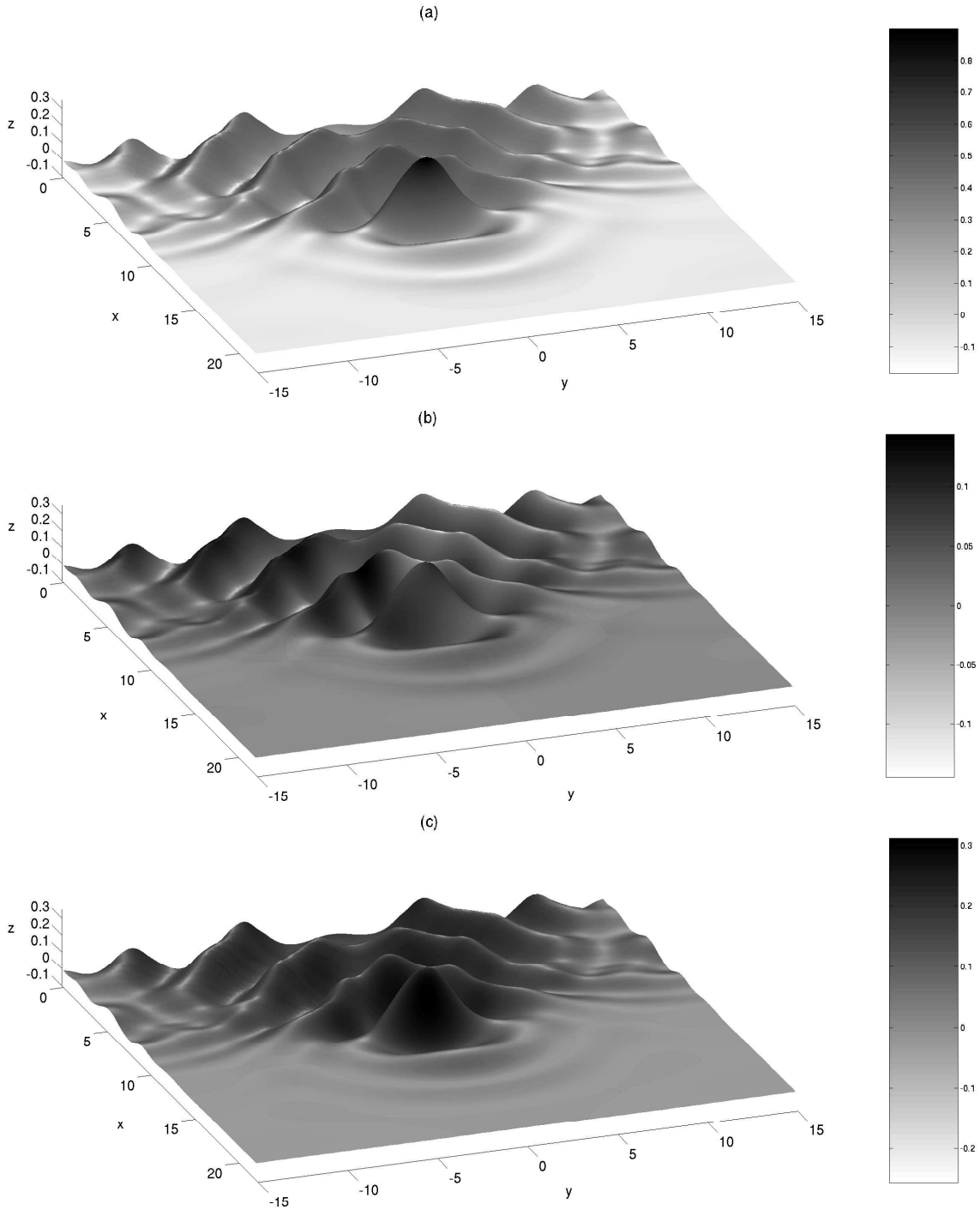

Fig. 10. Same case as Fig. 3d. Velocity field components on the free surface at $t = 6.89T$ (breaking time) : (a) u, (b) v, (c) w.

Finally, Fig. 11 shows a close-up of the development of the plunging jet at $t = 6.89T$. We did not attempt to accurately follow the overturning jet beyond this stage, in any of the applications reported in this work, although our model is capable of doing so, given a proper discretization [33]. Hence, we do not discuss wave breaking characteristics in detail, but limit our analyses to the initiation of breaking.

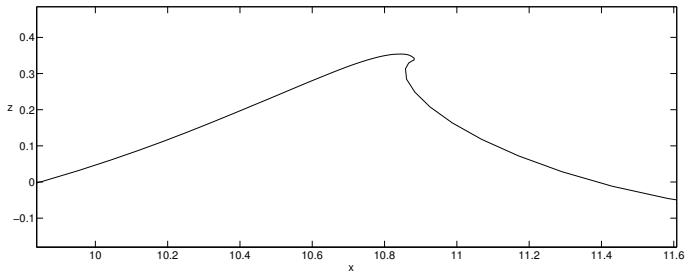

Fig. 11. Close-up of the overturning crest at $y = 0$ and $t = 6.89T$ for cases of Figs 4 and 7.

3.4 Parametric study

In the previous section, we presented detailed results for a typical 3D transient focused rogue wave, at the breaking point. Here, we study the effects of two parameters on the properties of focused waves: the maximum focusing angle of incident waves and the water depth. Due to the variations in parameters, we use nondimensional values in both the text and the figures, without specific symbol or notation to identify those. We compute nine cases for three values of the maximum focusing angle, $\theta_{max} = 40, 45, 50$ degrees, and three values of the water depth, $d = 1, 2, 3$. Most other parameters have identical values to those used in the first application. The only change deals with the stroke amplitude a of the paddles, which is adjusted such that the linear sum of the amplitudes of the generated waves, namely A^*, remains the same for all cases (Eq. 21), thus allowing a comparative study between these nine cases. For the waves generated in the previous application, which had a dimensionless wavelength $\lambda \simeq 3.90$, the water depth $d = 3$ clearly corresponds to deep water conditions, while the other two shallower depths correspond to intermediate water conditions.

Figure 12 shows free-surface elevations at the breaking point for the nine selected cases. Breaking clearly is a function of the two variable parameters. For a fixed water depth, a greater value of θ_{max} both increases the focal distance and delays the instant of breaking. For small θ_{max} values, wave components add together closer to the wavemaker leading to earlier breaking. For greater θ_{max} values, the focusing mechanism has more time to develop. Then we would have expected that, for such cases, focusing would periodically repeat itself in the middle of the tank, until a sufficiently large wave is generated and breaks. In fact, we observed that one of the first focused waves, after having gone through the theoretical focal point, keeps steepening and starts breaking, reaching a point of no-return. Hence, breaking

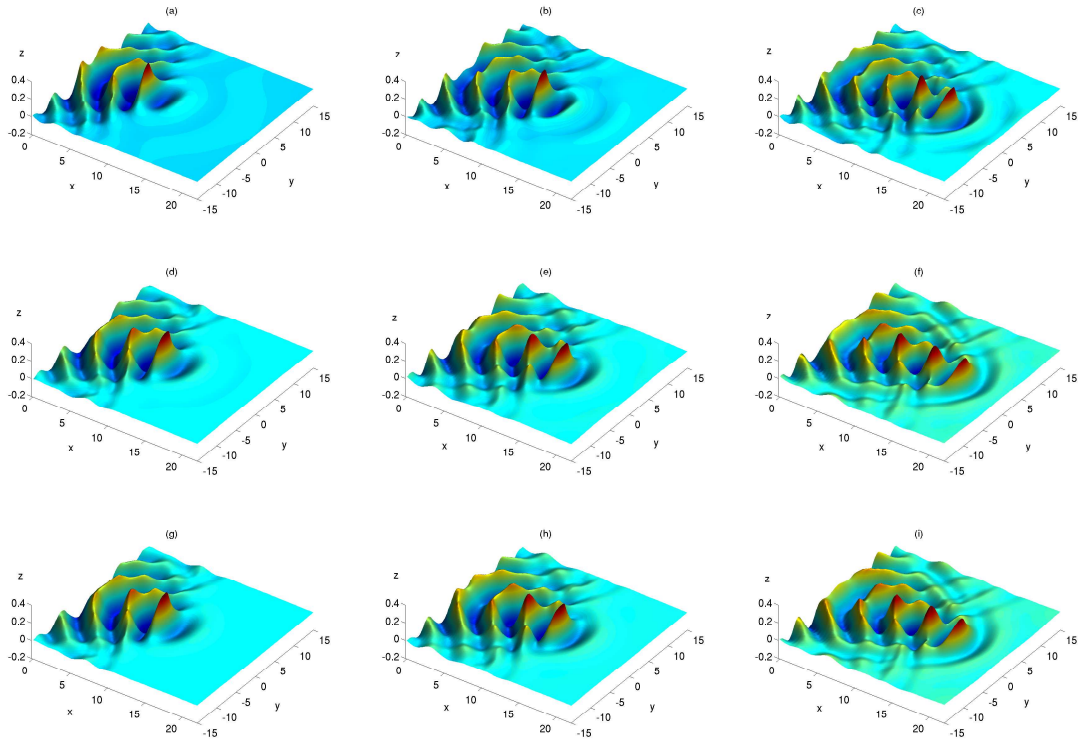

Fig. 12. Surface wave fields at breaking ($t = t_{BP}$): $d = 1$ and θ_{max} = (a) 40, (b) 45 and (c) 50; $d = 2$ and θ_{max} = (d) 40, (e) 45 and (f) 50; $d = 3$ and θ_{max} = (g) 40, (h) 45 and (i) 50. With: $A^* = 0.315$(6.3 m); $\Omega = 1.282$; $g = 1$; $N_\theta = 30$.

for these cases occurs during the defocusing stage (this is clear on Figs. 12c, f and i). Thus the key observation is that breaking does not necessarily occur when the maximum focusing amplitude is achieved. Different maximum focusing angles, i.e. directionality of incident waves, can lead to breaking at different stages of the focusing phenomenon. This has important implications for wave properties, as we shall see below. Regarding the effects of changes in water depth, we observe that the $d = 1$ cases, which correspond to shallower depth, lead to earlier breaking, whereas the intermediate ($d = 2$) and deep ($d = 3$) cases behave similarly.

Table 1 gives a list of wave characteristics computed for the nine test cases, based on 2D results measured in a vertical cross section at $y = 0$. Most of these characteristics are defined as in Bonmarin's paper [4] but, due to the observed rear-front asymmetry of the waves, we separately identified values related to both sides of the wave. Parameters δ and ϵ are obtained as A_c divided by the horizontal extension of the positive wave elevation to the rear or the front of the crest, respectively. The parameter s, which is similar to a parameter introduced in [25], is the ratio of the front crest length over the rear crest length, or $s = \epsilon/\delta$, and measures the vertical asymmetry of the crest.

The values of x_c and t_{BP} confirm what can be seen in Fig. 12 regarding the oc-

d	1	1	1	2	2	2	3	3	3
θ_{max}	40	45	50	40	45	50	40	45	50
t_{BP}	25.33	33.76	44.33	33.19	41.99	51.25	33.02	41.45	50.69
x_c	7.643	10.585	15.267	10.072	13.363	16.806	9.922	12.927	16.392
A_c	0.337	0.358	0.309	0.339	0.312	0.260	0.335	0.309	0.264
A_{t1}	0.164	0.180	0.168	0.194	0.189	0.167	0.196	0.192	0.169
A_{t2}	0.074	0.107	0.081	0.068	0.063	0.045	0.062	0.064	0.044
H_1	0.501	0.538	0.477	0.533	0.502	0.427	0.531	0.501	0.433
H_2	0.411	0.465	0.390	0.407	0.376	0.305	0.397	0.373	0.308
λ_1	4.062	4.075	3.808	4.226	4.101	3.801	4.266	4.096	3.824
λ_2	4.097	3.723	3.404	4.292	4.243	3.828	4.447	3.940	3.662
μ_1	0.673	0.666	0.648	0.637	0.623	0.609	0.631	0.617	0.610
μ_2	0.820	0.770	0.792	0.833	0.832	0.854	0.845	0.828	0.859
γ_1	0.123	0.132	0.125	0.126	0.122	0.112	0.125	0.122	0.113
γ_2	0.100	0.125	0.115	0.095	0.088	0.080	0.089	0.095	0.084
δ	0.392	0.360	0.374	0.346	0.390	0.405	0.350	0.339	0.391
ϵ	0.419	0.635	0.527	0.467	0.381	0.293	0.438	0.445	0.307
s	1.068	1.765	1.407	1.350	0.978	0.723	1.252	1.312	0.787
ℓ	3.030	3.298	4.062	3.876	4.198	4.496	3.852	4.178	4.430
ℓ/A_c	8.892	9.212	13.146	11.434	13.456	17.292	11.498	13.522	16.780

Table 1
Nondimensional wave characteristics at the breaking point $t = t_{BP}$ for parametric study: wave crest location x_c; crest amplitude A_c; trough amplitudes in the rear A_{t1} and in the front A_{t2}; wave heights in the rear $H_1 = A_{t1} + A_c$ and in the front $H_2 = A_{t2} + A_c$; wavelengths in the rear λ_1 and in the front λ_2; asymmetries in the rear $\mu_1 = A_c/H_1$ and in the front $\mu_2 = A_c/H_2$; wave steepness in the rear $\gamma_1 = H_1/\lambda_1$ and in the front $\gamma_2 = H_2/\lambda_2$; wave slope in the rear δ and in the front ϵ; vertical asymmetry s; wave width ℓ at $z = A_c/2$. The second column corresponds to the application detailed in Section 3.3.

currence of breaking. More precisely, we see that the deep water case is breaking slightly earlier than the intermediate one.

Table 1 shows that the amplitude parameters are essentially related to the focusing

or defocusing stage seen in Fig. 12. In this respect, the intermediate and deep water cases have very similar amplitude parameters. More specifically, A_c is larger when breaking occurs closer to the focal point. When breaking occurs during the defocusing stage, the wave crest amplitude is lower. The amplitudes A_{t1} and A_{t2} also depend on the location with respect to the focal point, but A_{t1} increases with d while A_{t2} decreases with d. H_2 appears to be the most consistent wave characteristic for explaining the effects of amplitude parameters: for each water depth, it is larger for cases where the wave crest and its front trough are the closest to the focal point; apart from this, we can deduce that H_2 decreases slightly as d increases.

The linear wavelength is 3.600, 3.815, and 3.825 for $d = 1$, 2, and 3, respectively. Wavelengths λ_1 and λ_2 show the same trend with d for the focusing cases, but are typically larger than the linear ones, due to nonlinear amplitude dispersion effects. For the defocusing cases, however, less predictable results are obtained. First we see that for ($d = 2$, $\theta_{max} = 50$), λ_1 is smaller than for ($d = 1$, $\theta_{max} = 50$): this is due to the defocusing evolution of the steepening wave. More surprising are the greater values of λ_2 for ($d = 2$, $\theta_{max} = 45, 50$) than for ($d = 3$, $\theta_{max} = 45, 50$), since we have seen that the $d = 2$ cases are slightly more "defocused" than the $d = 3$ cases. This observation means that these cases, which are similar in their evolution to breaking, have quite different breaking wave shapes.

For linear waves, both horizontal asymmetry parameters μ_1 and μ_2 are equal to 0.5. All our focused transient waves are strongly nonlinear, with a shallow front trough $A_{t2} \ll A_{t1}$ and, hence, a large μ_2 value. The asymmetry μ_1 shows an interesting trend: on the one hand, it decreases with increased θ_{max}; on the other hand, it increases for smaller depths. The latter makes sense due to the expected increase in asymmetry for shallower water waves.

Values of the rear steepness parameter γ_1 are quite constant for all cases, except for the two cases that are the most defocused. The front wave steepness γ_2 shows more variability, with larger values for smaller depth. The rear wave slope δ should quantify aspects of the breaking crest itself. This parameter value does not vary as much as the front wave slope ϵ. The vertical asymmetry factor s, equal to one in the linear approximation, is much larger for our test cases which are close to the focal point such as the cases ($d = 1$, $\theta_{max} = 45$), ($d = 2$, $\theta_{max} = 40$) and ($d = 3$, $\theta_{max} = 40$). However, when breaking occurs in a very defocused stage, this parameter may fall below one. In any case, it sems difficult to identify a clear trend for this parameter as a function of d, θ_{max}, and even the focusing/defocusing aspects. In particular, the intermediate and deep water cases have very different values for $\theta_{max} = 45$ while breaking at a similar slightly defocused stage.

The wave width parameter ℓ and the normalized width ℓ/A_c depend strongly on the focusing or defocusing stage at the instant of breaking. As expected, due to the directional mechanism of generation, these are minimal for cases that are breaking close to the focal point, whereas they are larger when the curved wave front focuses

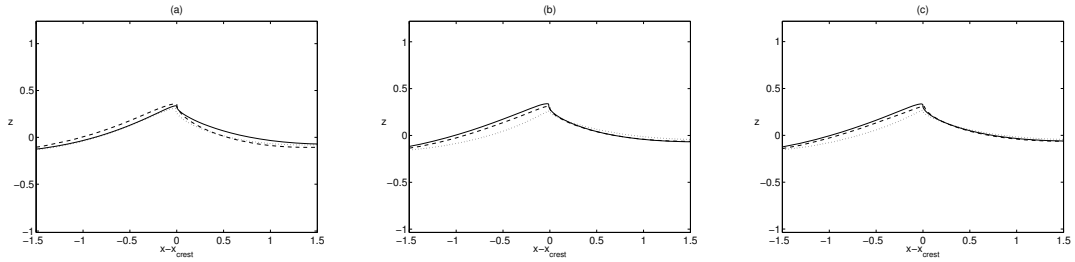

Fig. 13. Vertical cross-section ($y = 0$) at the breaking point ($t = t_{BP}$), for $\theta_{max} = 40$ (——); 45 (- - - - -); and 50 (. . . . .). (a) $d = 1$, (b) $d = 2$, (c) $d = 3$. The horizontal coordinates are shifted by x_c. No vertical exaggeration.

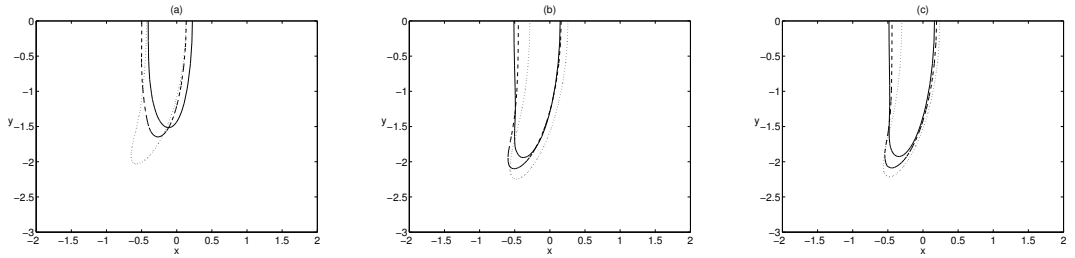

Fig. 14. Horizontal cross-section ($z = A_c/2$) at the breaking point ($t = t_{BP}$). Same definitions as for Fig. 13.

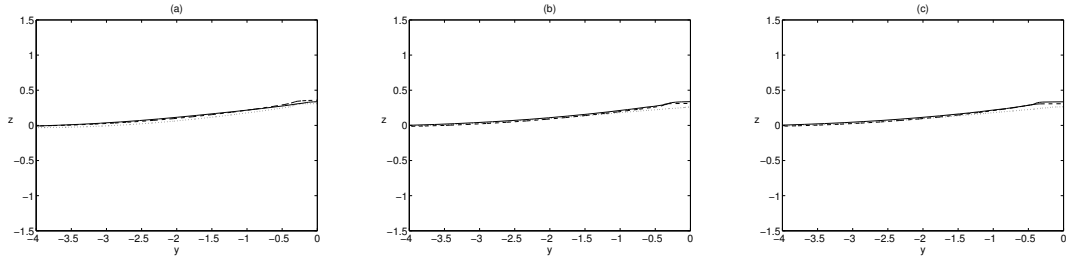

Fig. 15. Transverse cross-section ($x = x_c$) at the breaking point ($t = t_{BP}$). Same definitions as for Fig. 13. No vertical exaggeration.

or defocuses, while maintaining a large enough crest amplitude.

In order to better understand the effects of θ_{max} and d on the results, we show in Figures 13, 14 and 15 various cross-sections through the wave crest simulated for the nine test cases. The longitudinal cross-sections in Fig. 13 further illustrate the rear/front (or vertical) wave crest asymmetry (quantified by parameters δ, ϵ and s discussed before). After translating all sections to $x = x_c$, the crest geometry appears quite similar in most cases. The rear wave faces are quite straight and nearly parallel, which is consistent with the nearly constant value of δ, while the front faces are more curved, yielding quite different values of the asymmetry parameters ϵ and s (Table 1). As noted by Bonmarin [4], the deformation of the wave crest caused by impending breaking mostly affects the wave front face. By contrast, the two cases that are breaking at a very defocusing stage have a more deformed rear face (Fig. 13b,c). This gives a more symmetrical triangular shape to the breaking wave.

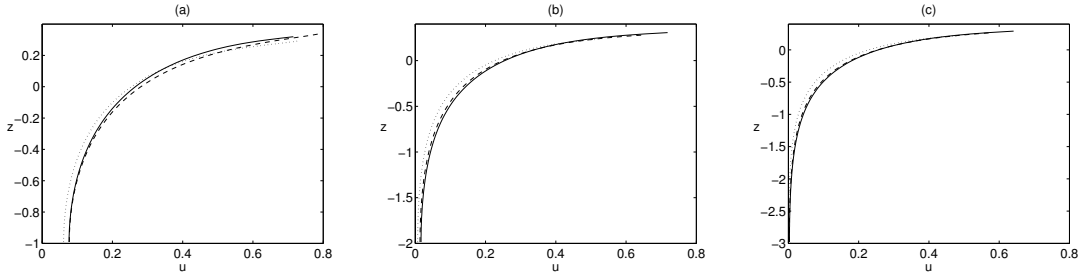

Fig. 16. Horizontal velocity u under the crest at breaking for $d =$ (a) 1, (b) 2, (c) 3. Same definitions as for Fig. 13.

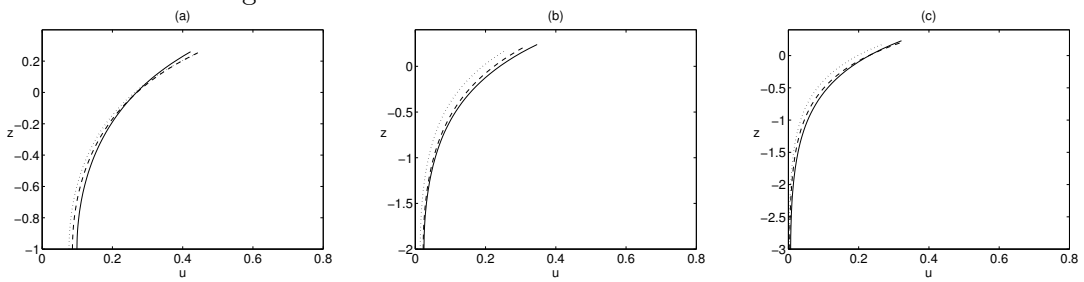

Fig. 17. Horizontal velocity u under the crest for a Stokes waves with the same height H_2 and wavelength λ_2 for $d =$ (a) 1, (b) 2, (c) 3.

Wave overturning in these cases is concentrated on a very small region of the crest (seemingly spilling breaking). Bonmarin further indicated that vertical asymmetry should increase with time in waves evolving towards breaking. However, this does not seem to apply when breaking occurs during the defocusing stage.

The horizontal cross-sections in Fig. 14 further show how the wave shape changes with respect to the focusing or defocusing situation. As expected from the discussion in the previous section, the curved wave front exhibits a crescent shape, with concavity oriented to the left or right, for defocusing or focusing cases, respectively. By contrast, the wave front shape is quite symmetrical (with respect to x) for cases close to focus. Figure 15 shows the transverse wave profiles at breaking, and confirms that the wave geometry is quite pyramidal. However, this pyramidal shape occurs just before breaking and is of short duration, since it was also noted that the wave shape tends to become more rounded again during the overturning.

Finally, we discuss wave kinematics at breaking. In the previous section we already presented and discussed internal velocity and acceleration fields for our first case (Figs. 4 to 9). Surface velocity fields were shown in Fig. 10 for the same case. Here, we analyze vertical variations of the horizontal velocity u and the vertical acceleration a_z under each wave crest at breaking, down to the bottom $z = -d$, in the plane $y = 0$, for the nine test cases (Figs. 16 and 18). Both of these essentially decrease gradually from crest to bottom. For the deepest water cases ($d = 3$), as expected, both reach nearly zero on the bottom and for a short distance above it. For the other two depth cases, there is a significant non-zero velocity on the bottom. Above the mean water level $z = 0$, horizontal velocities rapidly increase towards

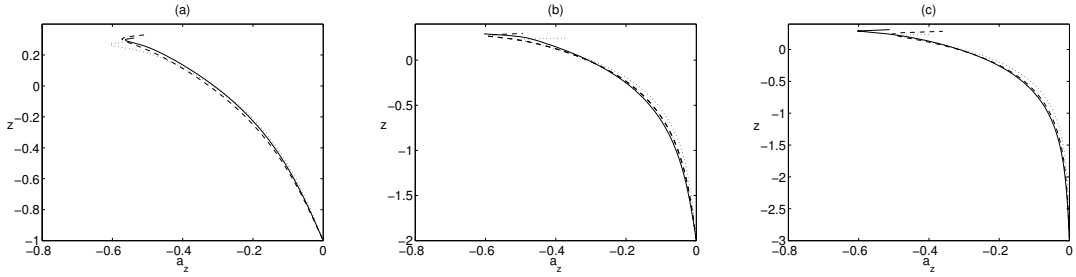

Fig. 18. Vertical acceleration a_z under the crest at breaking. Same definitions as for Fig. 16.

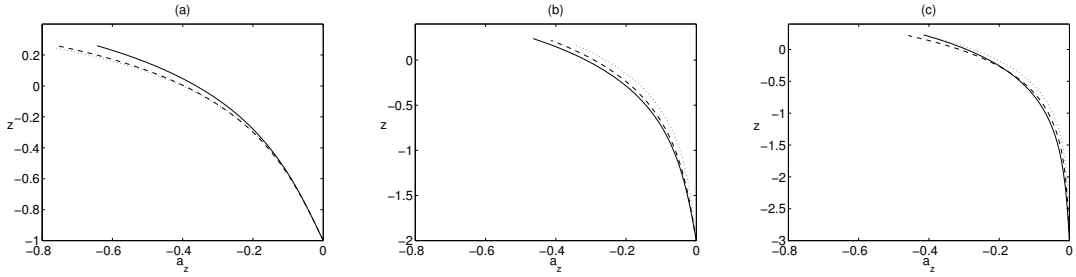

Fig. 19. Vertical acceleration a_z under the crest for an equivalent Stokes wave with the same height H_2 and wavelength λ_2 for $d =$ (a) 1, (b) 2, (c) 3.

the crest, even for the shallowest water cases ($d = 1$). While velocities differ only slightly between cases with $\theta_{max} = 40$ and $\theta_{max} = 45$, we observe that all cases with $\theta_{max} = 50$ have a smaller horizontal velocity between $z = -1$ and 0. Above $z = 0$, the curves for a given depth and different focusing angles are very close, especially for $d = 2$ and $d = 3$. For each depth, the maximum horizontal velocity is obtained for the highest wave (which corresponds to the case closer to the focal point). These maximum velocities are the greatest for the shallowest cases. In order to show the differences between the present waves and 2D Stokes waves, we computed the horizontal velocities for an equivalent Stokes wave with the same height H_2 and the same wavelength λ_2 using stream function theory (Fig.17) [12]. We see that all the vertical variations of horizontal velocity u under the crest look qualitatively similar. Much larger velocities (almost twice as large), however, occur in the high crest region in our focused transient 3D overturning waves than in the permanent form Stokes waves. Vertical accelerations, which provide a measure of non-hydrostatic pressure gradients, are significant over a large part of most diagrams. The largest accelerations are obtained for cases close to focus (excepted the ($d = 1$, $\theta_{max} = 50$) defocusing case, which provides a slightly greater maximum vertical acceleration than the two other cases for the same depth). The maximum value obtained for each depth among the three different θ_{max} cases is roughly 0.6 for any depth. Thus, the water depth has not a great influence on these maximum values in our numerical experiments. We also see, in most cases, a decrease of the vertical acceleration in the upper crest. For ($d = 2$, $\theta_{max} = 40$), this decrease is not visible and the vertical acceleration seems to monotonously increase towards the crest; this however is likely due to an insufficient number of points under the crest in the computations, while the decrease only occurs in a very thin zone close to the crest. Fig.19 shows the vertical

acceleration for equivalent Stokes waves. In the shallower cases, the accelerations are larger in the Stokes waves, while for other depths ($d = 2$ and $d = 3$), it is the opposite. The influence of the water depth is quantitatively significative: this emphasizes the opposite observation of globally similar maximum values for any depth that we made from Fig.18. In the Stokes waves, one does not obtain the reversal of acceleration close to the crest, which may in part explain why horizontal velocities stay smaller near the crest. Note that, the series representation of the kinematics in the laterally symmetric Stokes waves, would not allow for such a behavior to be expressed, even if the physics called for it.

4 Conclusions

We studied the generation of overturning rogue waves by directional energy focusing in a fully nonlinear potential flow model, with the purpose of analyzing their geometry and kinematics. The model is based on a high-order BEM, recently made more efficient by the implementation of a Fast Multipole Algorithm, which computes all matrix-vector products related to the discretization [19]. In the applications, waves are generated in a 3D Numerical Wave Tank (NWT) by simulating the movement of a snake wavemaker. Brandini and Grilli [7] presented a similar study based on an earlier version of the NWT. They could not, however, reach the overturning phase for an extreme wave event, both due to limitations in the model implementation (now corrected; see Fochesato *et al.*, 2005) and discretization size that could be realistically achieved. By contrast, in this work, we usually resolve wave focusing well enough to accurately create large scale plunging breakers in the NWT. Thus, we perform a parametric study of wave properties at the onset of breaking, by testing three water depths and three maximum angles of directional focusing. We specifically analyze the 3D geometry and kinematics of such waves and make observations on their dependence to governing parameters.

The main features of rogue waves observed in our results are as follows. A vertical 2D longitudinal (x) cross-section through an extreme wave crest looks quite similar to the characteristic shape observed for rogue waves in the ocean: a tall and steep doubly asymmetric wave crest occurs, in between two shallower troughs. Maximum wave steepness and slope at focusing as well as the horizontal velocity in the crest are larger than those of a limiting periodic wave that has no rear/front asymmetry. Unlike in Bonmarin's observations [4], we find that the vertical asymmetry factor does not necessarily increase with time, the steepening mostly occurring in the upper crest. We agree with [4], however, that the deformation of the crest at breaking mostly affects the wave front face, the back face being quite straight and having nearly the same slope for all cases.

The 3D wave generation yields a curved wave front before focusing occurs. A shallow circular trough forms in front of the focused wave (i.e., the "hole in the sea"), fol-

lowed by a deeper trough, with a crescent shape. The 3D shape of the focused wave appears to be almost pyramidal, for a small time prior to breaking. By contrast, during the focusing phase as well as the development of overturning, the transverse shape of the wave, through the crest, tends to have a more rounded shape. Wave kinematics exhibits two main phases. First, we observe the propagation of a curved crest line, converging towards a small area of the NWT. When the focused wave is generated, it steepens, and flow velocity and acceleration vectors have weak transverse components near the front face of the wave. Hence, after a 3D focusing phase, wave overturning and breaking become locally quasi-2D. This may help explain observations of a moving "wall of water", reported in some stories of rogue waves in the ocean. Other findings regarding wave kinematics are: (i) horizontal velocities are very non-uniform over depth, steeply increasing under the wave crest, even for the shallowest water cases; (ii) vertical acceleration and, hence, non-hydrostatic pressure gradients, are always significant under the crest; (iii) the largest horizontal velocities at the crest are obtained when wave overturning occurs close to the focal point; (iv) the largest vertical accelerations are weakly dependent on the water depth, unlike what we find for Stokes waves of identical height and wavelength; and (v) maximum accelerations occur slightly below the free surface, under the crest. In this respect, kinematics in our focusing overturning 3D waves, despite their quasi-2D nature, is found to be quite different from that in Stokes waves of identical height and wavelength. Horizontal velocity near the crest, in particular, is found to be twice as large. Considering Stokes waves are often used as a model for extreme waves in the offshore industry, the strong underprediction of kinematics they lead to is an important finding that may help improve the design of offshore structures against rogue wave impact [10].

It has been difficult to find general trends for the influence of water depth and maximum focusing angle of incident waves, on geometrical and kinematic parameters at the breaking point. This is because the former parameters significantly modify conditions under which waves break. For instance, a smaller depth or a larger maximum angle significantly delay the onset of breaking. Thus, breaking can occur during focusing, nearly at the focal point, or during the defocusing stage. This "displacement" of the breaking point has a much greater influence on wave characteristics than the values of the governing parameters themselves (i.e., depth or angle). A statistical approach based on a much large number of numerical experiments could probably provide more quantitative information on the exact influence of these two parameters. This could be the object of future work. Another future study would be to focus many more smaller wave components to create the rogue wave, and vary the amplitude of those, such that only one very large wave appears in the NWT and eventually starts to break, rather than a series of waves of gradually increasing height, as we have here. Our method was appropriate since we were more interested in the kinematics of a deterministically generated rogue wave, rather than on finding new mechanisms for rogue wave generation itself. Our 3D-NWT, however, is general and more complex numerical experiments could be performed in the future, featuring more realistic rogue wave generation mechanisms.

Acknowledgments

The source codes used to compute the Stokes wave kinematics based on the Fourier series decomposition of the stream function (the so-called "stream function theory") have been provided by Michel Benoit from EDF R&D, Laboratoire National d'Hydraulique et Environnement (LNHE) in Chatou (France). His contribution is gratefully acknowledged.

References

[1] Benjamin T.B., Feir J.E. : The disintegration of wave trains on deep water. Part 1. Theory, *J. Fluid Mech.* **27**, 417–430, 1967.

[2] Biausser B., Grilli S.T., Fraunié P. : Numerical simulations of three-dimensional wave breaking by coupling of a VOF method and a boundary element method, *Proc. 13th Offshore and Polar Engng. Conf.* (ISOPE 2003), Honolulu, USA, 333–339, 2003.

[3] Biausser B., Grilli S.T., Fraunié P., Marcer R. : Numerical analysis of the internal kinematics and dynamics of three-dimensional breaking waves on slopes, *Intl. J. Offshore and Polar Engng.* **14**(4), 247–256, 2004.

[4] Bonmarin P. : Geometric properties of deep-water breaking waves, *J. Fluid Mech.* **209**, 405–433, 1989.

[5] Bonnefoy F., Le Touze D., Ferrant P.: Generation of fully-nonlinear prescribed wave fields using a high-order spectral method, *Proc. 14th Offshore and Polar Engng. Conf.* (ISOPE 2004), Toulon, France, **3**, 257–263, 2004.

[6] Brandini C.: Nonlinear interaction processes in extreme wave dynamics, Ph.D. Dissertation, University of Firenze, 2001.

[7] Brandini C., Grilli S.: Modeling of freak wave generation in a 3D-NWT, *Proc. 11th Offshore and Polar Engng. Conf.* (ISOPE 2001), Stavanger, Norway, **3**, 124–131, 2001.

[8] Chaplin J.R.: On frequency-focusing unidirectional waves, *Intl. J. Offshore and Polar Engng.* **6**, 131–137, 1996.

[9] Clément A.: Coupling of two absorbing boundary conditions for 2D time-domain simulations of free surface gravity waves, *J. Comp. Phys.* **26**, 139–151, 1996.

[10] Corte, C. and Grilli S.T.: Numerical Modeling of Extreme Wave Slamming on Cylindrical Offshore Support Structures. In *Proc. 16th Offshore and Polar Engng. Conf.* (ISOPE 2006), San Francisco, USA, **3**, 394-401, 2006.

[11] Dalrymple R.A.: Directional wavemaker theory with sidewall reflection, *J. Hydraulic Res.* **27** (1), 23–34, 1989.

[12] Dean, R.G. and Dalrymple R.A. *Water Wave Mechanics for Engineers and Scientists* Prentice-Hall, 1984.

[13] Dias F., Bridges T.: The numerical computation of freely propagating time-dependent irrotational water waves, *Fluid Dyn. Research* **38**, 803–830, 2006.

[14] Dommermuth D.G., Yue D.K.P., Lin W.M., Rapp R.J., Chan E.S., and Melville W.K.: Deep-water plunging breakers : a comparison between potential theory and experiments, *J. Fluid Mech.* **189**, 423–442, 1998.

[15] Ducrozet G. , Bonnefoy F. , Le Touzé D., and Ferrant P. : 3D HOS simulations of extreme waves in open seas, *Natural Hazards and Earth System Sciences* (submitted), 2006.

[16] Ducrozet G. , Bonnefoy F. , Le Touzé D., and Ferrant P. : Implementation and Validation of Nonlinear Wave Maker Models in a HOS Numerical Wave Tank, *International Journal of Offshore and Polar Engineering*, **16**, 161167, 2006.

[17] Duncan J.H.: Spilling breakers *Ann. Rev. Fluid Mech.* **33**, 519–547, 2001.

[18] Dyachenko A.I., and Zakharov V.E.: Modulation instability of Stokes wave – Freak wave, *JETP Letters* **81**, 255–259, 2005.

[19] Fochesato C. and Dias F. : A fast method for nonlinear three-dimensional free-surface waves, *Proc. Roy. Soc. Lond. A* **462**, 2715–2735, 2006.

[20] Fochesato, C., Grilli, S. and Guyenne P.: Note on non-orthogonality of local curvilinear co-ordinates in a three-dimensional boundary element method, *Intl. J. Num. Meth. Fluids* **48**, 305–324, 2005.

[21] Fuhrman D.R., and Madsen P.A.: Numerical simulation of extreme events from focused directionally spread wavefields *Proc. 30th Intl. Conf. Coastal Engng.* (ICCE30, September 2006, San Diego, California) (in press), 2006.

[22] Graziani G., and Landrini M.: Application of multipoles expansion technique to two-dimensional nonlinear free-surface flows, *J. Ship Research* **43**, 1–12, 1999.

[23] Greengard L.: *The Rapid Evaluation of Potential Fields in Particle Systems,* MIT Press, Cambridge, MA, 1988.

[24] Greengard L., and Rokhlin V.: A fast algorithm for particle simulations, *J. Comput. Phys.* **73**, 325–348, 1987.

[25] Grilli, S.T. : Depth inversion in shallow water based on nonlinear properties of shoaling periodic waves, *Coastal Engineering*, **35**(3), 185-209, 1998.

[26] Grilli S., Guyenne P., and Dias F.: A fully nonlinear model for three-dimensional overturning waves over arbitrary bottom, *Int. J. Num. Meth. Fluids* **35**, 829–867, 2001.

[27] Grilli S.T., and Horrillo J.: Numerical generation and absorption of fully nonlinear periodic waves, *J. Engng. Mech.* **123** (10), 1060–1069, 1997.

[28] Grilli S.T., Subramanya R., Svendsen I.A., and Veeramony J.: Shoaling of Solitary Waves on Plane Beaches, *J. Waterway, Port. Coastal, Ocean Engng.* **120**, 609–628, 1994.

[29] Grilli S.T., Svendsen I.A., and Subramanya R.: Breaking criterion and characteristics for solitary waves on slopes, *J. Waterway, Port. Coastal, Ocean Engng.* **123**, 102–112, 1997.

[30] Grilli S.T., Svendsen I.A., and Subramanya R.: Closure of : Breaking criterion and characteristics for solitary waves on slopes, *J. Waterway, Port. Coastal, Ocean Engng.* **124**, 333–335, 1998.

[31] Grilli S. and Watts P.: Modeling of tsunami generation by an underwater landslide in a 3D-NWT, *Proc. 11th Offshore and Polar Engng. Conf.* (ISOPE 2001), Stavanger, Norway, 2001.

[32] Grue J., Clamond D., Huseby M., and Jensen A.: Kinematics of extreme waves in deep water, *Appl. Ocean Res.* **25**, 355–366, 2003.

[33] Guyenne, P. and Grilli, S.T.: Numerical study of three-dimensional overturning waves in shallow water, *J. Fluid Mech.* **547**, 361-388, 2006.

[34] Hague C.H., and Swan C., : Numerical Simulations of Large Deep Water Waves: The Application of a Boundary Element Method, *Proc. 25th Intl. Conf. Offshore Mech. and Arctic Engng.* (OMAE2006, June 2006, Hamburg, Germany), 2006.

[35] Haver, S. and Andersen, O.J.: Freak waves: rare realizations of typical population or typical realization of a rare population ?, *Proc. 10th Offshore and Polar Engng. Conf.* (ISOPE 2000), Seattle, USA, **3**, 123–130, 2000.

[36] Henderson, K.L., Peregrine, D.H. and Dold, J.W.: Unsteady water wave modulations: fully non linear solutions and comparison with the nonlinear Schrödinger equation, *Wave Motion* **9**, 341–361, 1999.

[37] Johannessen T.B., and Swan C.: A laboratory study of the focusing of transient and directionally spread surface water waves, *Proc. Roy. Soc. Lond.* **457**, 971–1006, 2001.

[38] Kharif C. and Pelinovsky E.: Physical mechanisms of the rogue wave phenomenon, *Eur. J. Mech. B/Fluids* **22**, 603–634, 2003.

[39] Kjeldsen S.P.: Measurements of freak waves in Norway and related ship accidents, *Proc. Rogue Waves 04*, Brest, France, 2005.

[40] Korsmeyer F.T., Yue D.K.P., Nabors K.: Multipole-Accelerated Preconditioned Iterative Methods for Three-Dimensional Potential Problems, presented at *BEM 15*, Worcester, MA, 1993.

[41] Lachaume C., Biausser B., Grilli S.T., Fraunie P., and Guignard S.: Modeling of breaking and post-breaking waves on slopes by coupling of BEM and VOF methods, *Proc. 13th Offshore and Polar Engng. Conf.* (ISOPE 2003), Honolulu, USA, 353-359, 2003.

[42] Lubin P., Vincent S., Caltagirone J.-P., and Abadie S.: Fully three-dimensional direct numerical simulation of plunging breaking waves *C. R. Mécanique*, **331**, 495–501, 2003.

[43] Mallory, J.K.: Abnormal waves on the south east coast of South Africa, *Intl. Hydrog. Rev.* **51**, 99-129, 1974.

[44] McLean, J.W.: Instabilities and breaking of finite amplitude waves, *J. Fluid Mech.*, **114**, 331-341, 1982.

[45] Nishimura N.: Fast multipole accelerated boundary integral equation methods, *Appl. Mech. Rev.* **55**, 299–324, 2002.

[46] Rokhlin V.: Rapid solution of integral equations of classical potential theory, *J. Comput. Phys.* **60**, 187–207, 1985.

[47] Scorpio S., and Beck F.: A Multipole Accelerated Desingularized Method for Computing Nonlinear Wave Forces on Bodies, presented at *15th Intl. Conf. Offshore Mech. Arctic Engng.*, Florence, Italy, 1996.

[48] She K., Greated C.A., and Easson W.J. : Experimental study of three-dimensional wave breaking, *J. Waterway, Port. Coastal, Ocean Engng.* **120**, 20–36, 1994.

[49] She K., Greated C.A., and Easson W.J.: Experimental study of three-dimensional breaking wave kinematics, *Appl. Ocean Res.* **19**, 329–343, 1997.

[50] Srisupattarawanit T., Niekamp R., and Matthies H.G.: Simulation of nonlinear random finite depth waves coupled with an elastic structure, *Comput. Methods Appl. Mech. Engrg.* **195**, 3072–3086, 2006.

[51] Su M.Y., Bergin M., Marler P., and Myrick, R.: Experiments on nonlinear instabilities and evolution of steep gravity-wave trains, *J. Fluid Mech.*, **124**, 45-72, 1982.

[52] Zakharov V.E., Dyachenko A.I., and Prokofiev A.O.: Freak waves as nonlinear stage of Stokes wave modulation instability, *Eur. J. Mech. B/Fluids* **25**, 677–692, 2006.